Chemical evolution of polycrystalline cementite (Fe_3C) during single-pass sliding wear: an investigation by surface spectroscopy

Hanna Tsybenko[1], J. Manoj Prabhakar[2], Michael Rohwerder[2], Gerhard Dehm[1], Steffen Brinckmann[1,3]

[1] Department Structure and Nano-/Micromechanics of Materials, Max-Planck-Institut für Eisenforschung GmbH, Düsseldorf, Germany

[2]Department Interface Chemistry and Surface Engineering, Max-Planck-Institut für Eisenforschung GmbH, Düsseldorf, Germany

[3] Microstructure and Properties of Materials (IEK-2), Forschungszentrum Jülich, Jülich, Germany

Abstract

The development of wear-resistant steels requires an understanding of deformation behavior and chemical evolution in cementite (Fe_3C) under tribological loading. Previous investigations of chemical changes in steels during wear provided limited knowledge of the cementite stability and its transformations as the single phase is conventionally embedded in a metal matrix. This study examines elemental and phase distributions in bulk polycrystalline cementite with minor fractions of graphite, iron, and wüstite after single-pass sliding wear. We employ energy-dispersive X-ray spectroscopy in scanning transmission electron microscope, Auger electron spectroscopy, and X-ray photoelectron spectroscopy to characterize cementite composition before and after wear. Our results demonstrate that severe plastic deformation via contact shear leads to the partial decomposition and mechanical mixing of the non-cementite inclusions into the cementite matrix and the partial elemental homogenization in the outermost deformed region. In addition, we relate the dissolution of the graphite, which is present in the initial microstructure, to the formation of the Hägg carbides (Fe_5C_2).

Keywords

Cementite, sliding wear, phase transformation, Hägg carbide

1 Introduction

Due to their high wear resistance, multiphase pearlitic, bainitic and martensitic steels are often used for tribological applications, e.g., bearings, rails, and train wheels. The wear performance of such steels is generally improved by the strengthening via the cementite phase (Fe_3C) [1,2]. In pearlite, the cementite leads to the stabilization of the plasticity in ferrite during the initial loading stages [3,4]. In addition, the continuous microstructure refinement during deformation increases the ferrite-cementite interface density and thus significantly restricts dislocation motion [5–7]. In bainitic and martensitic steels with large spheroidized cementite particles, the matrix flow is constrained by these cementite inclusions, resulting in locally increased stresses at the interfaces [8,9]. Solid solution strengthening is achieved by cementite dissolution into the matrix phase at high strains [9–14]. Nonetheless, cementite dissolution during wear is also associated with the formation of the brittle carbon-saturated white etching layers/areas, which are responsible for fracture and rapid erosion in the contact region [8,15–18].

For the development of more wear-resistant steels, the tribological behavior of the cementite phase has to be well understood. Since the microstructure and chemical evolution are partially determined by the cementite interaction with the surrounding matrix (e.g., ferrite, martensite) in the multiphase steels, one cannot focus on the individual mechanisms in Fe_3C. To this end, we characterize the wear properties of cementite by investigating bulk polycrystalline samples with minor fractions of graphite and iron oxide produced by spark

plasma sintering [19]. The present research mainly focuses on the abrasive wear properties of Fe_3C. In the work of Sasaki et al. [20], the two-body wear performance of polycrystalline cementite was compared to pure iron, commercial steel, and other sintered cementite-iron samples. During their pin abrasion experiments at varying apparent applied pressures, bulk cementite demonstrated the best abrasive wear resistance among all analyzed materials up to apparent applied pressures of 0.61 MPa, whereas at 1.23 MPa, the 100 vol.% cementite sample demonstrated higher wear volume loss than the 75 vol.% cementite [20]. In three-body wear experiments in block-on-ring geometry with SiC abrasives on pure iron and sintered iron-cementite samples, Zheng et al. [21] reported the smallest wear weight loss for bulk cementite up to applied pressures of 0.065 MPa. At the applied pressure of 0.098 MPa, fracture became the predominant deformation mechanism, and the wear weight loss significantly increased correspondingly. The calculation of the applied pressures was not described in the abovementioned studies, and the principles of the pin abrasion, as well as block-on-ring experiments, differ considerably from the microscale wear experiments conducted in this work. Nonetheless, the first experimental studies have demonstrated the importance of investigating the deformation behavior of cementite under various wear conditions.

It is essential, however, to relate the wear performance of cementite to its underlying deformation behavior and chemical evolution during tribological loading. In our previous study [21], the deformation mechanisms of bulk cementite during single-and multi-pass sliding wear were investigated. We reported that cementite tends to form a layered, deformed microstructure during sliding wear. Due to the enhanced ductility, bulk polycrystalline cementite deforms plastically below the contact surface by dislocation slip, shear band formation, fragmentation, grain boundary sliding, and grain rotation. In addition, brittle fatigue crack formation was observed for multi-pass experiments. The deformed microstructure resulted in a significant increase in the nanoindentation hardness [21].

Since the main aim of the previous work was to unravel the deformation mechanisms of cementite in the contact region, the effect of tribological loading on the chemical evolution was only marginally addressed. In particular, the Hägg carbide formation in the outermost layer of the wear track was detected [21]. Hägg carbide (Fe_5C_2) is the most stable transition carbide before a stable mixture of iron and cementite forms during high-carbon martensite tempering [22]. Hägg carbide precipitates can either coexist with cementite or grow at the cost of cementite at sufficiently high carbon concentrations [23–28]. Therefore, the formation of Hägg carbides in the contact region indicates the existence of carbon gradients, which provide a driving force for precipitation. Initial results suggested two possible explanations for the excess carbon that promotes phase transformation: decomposition of graphite particles and oxidation of cementite during wear [21]. However, more evidence is required to provide conclusive support for one of the suggested mechanisms.

This study investigates the tribological behavior of sintered polycrystalline cementite with minor fractions of graphite and iron oxide [19] and focuses on the chemical evolution during single-pass sliding wear. We employ energy-dispersive X-ray spectroscopy in scanning transmission electron microscope (STEM-EDS), Auger electron spectroscopy (AES), and X-ray photoelectron spectroscopy (XPS) to analyze the elemental and phase composition of the deformed layers of the sample as well as of the undeformed regions. By combining these surface spectroscopy techniques, we aim to show the correlation between the deformation-related microstructure changes and the qualitative and semi-quantitative differences in the elemental and phase distributions. Based on the results of this study, we validate the proposed sources for carbon enrichment in the outermost deformed region and determine feasible mechanisms for the cementite to Hägg carbide phase transformation.

2 Experimental procedure

2.1 Material and sample preparation

The bulk polycrystalline cementite samples (courtesy of Prof. Y. Todaka of the Toyohashi University of Technology) were fabricated from Fe (99.9%) and C (99.9%) powders and mixed in a 3:1 ratio. The powders underwent mechanical alloying for 20 h in a vibration ball mill in an argon atmosphere. During the final step, the samples were spark plasma sintered at 50 MPa at 900°C for 15 min, as described by Umemoto et al. [19]. A remnant porosity was observed after the sintering, and the relative density was measured as 98% [19]. The as-received cementite sample was mechanically polished using the 3 µm and the 1 µm polycrystalline diamond suspensions (Struers) and a colloidal silicon oxide polishing suspension (OPS, Struers). The resulting average surface roughness was determined as ~10 nm by a line scan with 0.15 mN normal force in a nanoindenter before the wear experiment [29].

Based on the initial phase composition analysis by X-ray diffraction (XRD), the sample consists of 94.5 vol.% cementite (95 wt.%), 2.9 vol.% iron (3 wt.%), and 2.6 vol.% wüstite FeO (2 wt.%) [21]. Previous observations [19,21] confirmed the presence of finely dispersed graphite after the spark plasma sintering (Fig. A1). Fig. A2 in the Appendix A shows the measurements of the non-cementite particles in the sintered polycrystalline sample using EDS.

2.2 Wear experiments

Microscale sliding wear experiments were performed in a KLA (Agilent, Keysight) G200 Nanoindenter using a sphero-conical diamond tip with a 5 µm radius (Synton-MDP). At the beginning of the experiment, the tip gradually indents the sample until a pre-defined normal load of 100 mN is reached. Then, the sample is moved laterally under the constant velocity of 10 µm/s [30,31]. The nanoindentation hardness and the scratch hardness of bulk cementite were determined previously as 11.1 GPa and 14.8 GPa, respectively [29]. Assuming a half-circular contact area during wear, the loading conditions thus correspond to the contact depth of 0.45 µm [21]. As a result, the wear experiments led to severe plastic deformation in the contact region as well as to phase transformation in the outermost deformed layer [21].

In order to perform XPS measurements on the scratched cementite surface, we conducted multiple parallel microscale scratch experiments in close proximity (wear track array). The loading conditions were the same as during the single wear track experiments previously described. Thus, a high fraction (~92%, Fig. A3 in the Appendix A) of the sample surface area (800 x 800 µm) was covered with wear tracks. It should be pointed out that the plastically deformed zones are much larger than the wear track grooves. Therefore, the effect of the remaining 8% non-groove surfaces on the measurements is much less than the 92% wear track groove fraction, and we assume that the former surface regions have a neglectable influence on the XPS results.

2.3 Chemical composition characterization

A wear track groove was imaged in a Zeiss Gemini scanning electron microscope (SEM) with a secondary electron detector. In order to perform STEM and EDS studies, a cross-section specimen was lifted out in a Thermo Fisher Scientific Scios 2 DualBeam focused ion beam (FIB)-SEM system with a Ga^+ ion source at a 30 kV acceleration voltage. The beam current was 1.6 nA during the initial milling steps and was gradually decreased down to 10 pA for the polishing and cleaning step after the specimen thickness reached 100 nm.

STEM-EDS analysis was conducted in a JEOL JEM-2200FS microscope operated at a 200 kV acceleration voltage. EDS results provide information on the composition at the specific position and thus are dependent on the

measurement location. The precise atomic concentrations are difficult to evaluate due to the spurious X-rays mainly originating from the objective pole piece in the transmission electron microscope (TEM), as well as due to the carbon and oxygen contamination of the specimen surface from the atmosphere. Therefore, EDS provides not the real compositions of studied phases but allows for the semi-quantitative analysis of the relative elemental differences in the studied areas. Hence, the results of the EDS analysis are discussed qualitatively. However, care was taken that all EDS measurements were performed under identical conditions. The following acquisition parameters were used for the measurement: 7.475 nA probe current, 71 min total acquisition time, and 8 min dead time. For the quantification of peaks, k-factors of 2.072, 1.1453, 1, 1.2762, 2.9773, and 2.401 were applied for C, O, Fe, Cu, Ga, and Pt, respectively. Due to the sample milling with Ga^+ ions, mounting on a Cu grid, and Pt protective coating, additional gallium (~0.1 at.%), copper (~5 at.%), and platinum (~0.1 at%) signals are observed in the EDS line profiles. Fig. A4 in the Appendix A demonstrates the overall EDS spectrum from the region of interest and detected elements.

Auger spectra with a spot size of ~0.5 x 0.5 µm were acquired inside and outside the wear track groove using a ULVAC-PHI 710 scanning auger microprobe (SAM). During these measurements, the primary beam energy was 15 kV. Sputtering with 1kV Ar^+ ions during Zalar rotation was performed to obtain AES spectra at different depths for a maximum duration of 210 min. SEM images of the wear track surface obtained after the final sputtering step indicate the removal of approx. 400 nm thick layer (Appendix A, Fig. A5). The obtained Auger spectra are then studied qualitatively to determine the presence of different carbon compounds before and after deformation.

XPS spectra were recorded on the wear track array and undeformed surface using a PHI Quantera II spectrometer with an Al-Kα source. The beam size was set to 100 µm. Probing a large area is advantageous because local sample inhomogeneities do not impact the results in these measurements as much as they would if a small beam size were used. In these investigations, we focus on systematic composition differences. We employed a pass energy of 112 eV and an energy step size of 0.2 eV for the spectra acquisition of the survey scan. To obtain the core level spectra of iron (Fe 2p), carbon (C 1s), and oxygen (O 1s), pass energies of 55 eV, 26 eV, and 26 eV, as well as energy step sizes of 0.05 eV, 0.025 eV, and 0.025 eV were used, respectively. In all measurements, the take-off angle was set to 45°. To perform depth profiling, 500 eV Ar^+-ion beam of size 1mm x 1mm was used to sputter the studied areas in a step-wise fashion with an overall duration of 1026 s. The sputtering rate was assumed as ~35 nm/min by correlating with a sputter calibration done on a silica sample, leading to an overall sputtered depth of 600 nm. Calibration on two samples with high cementite, ferrite, and graphite fractions was conducted prior to analyzing the results obtained from the polycrystalline cementite sample to ensure the optimal peak fitting and allow for more accurate quantification of elemental and phase compositions of the sample (Appendix A, Fig. A6, A7).

We performed the peak fitting using the CasaXPS 2.3.22 software. The Shirley-type backgrounds were subtracted for all spectra. For the asymmetric metallic iron peak, the LA(1.2,4.8,3) peak shape was fitted, whereas a Gaussian (70 %) - Lorentzian (30 %) peak shape was used for the symmetric components [32]. For the Fe 2p3/2 spectra, the following components were fitted: Fe-metal at 706.7 eV, Fe-carbide at 707.1 eV, Fe_3O_4/FeO (Fe2+) at 708.8 eV, Fe_2O_3 (Fe3+) at 710.5 eV and Fe_2O_3-satellite at 711.6 eV. The literature on XPS characterization of iron carbides is scarce. In some studies, the binding energy for Fe-cementite was reported as 708.2 eV [33–35], whereas other works mention values similar to that of metallic Fe, i.e., 707.2-707.3 eV [36,37] due to the metallic-covalent bonding. We adjusted the position of the cementite peak to 707.1 eV based on the Fe 2p3/2 spectra of the undeformed cementite at the end of the sputtering period (1026 s) because we expect the cementite iron peak to be dominant in this case. This binding energy is similar to the

one reported for Fe-Hägg carbide, i.e., 707.0-707.3 eV [38,39], and therefore we use a single peak for fitting both Fe-carbide compounds. The C 1s spectra were typically assigned to the carbidic C at 283.5 eV and graphitic C at 284.9 eV. Literature gives the binding energies in the range of 283.2-283.6 eV for the carbidic C peak (cementite, Hägg carbide) [34,39–42]. To account for the carbon contamination during sample preparation and storage, further C peaks were fitted into the C 1s spectra that were measured before and after the initial sputtering steps: Ca_2C at 282.0 eV, C-O at 286.2 eV, C=O at 287.4 eV, O-C=O at 288.7 eV, and $CaCO_3$ at 289.7 eV [35]. The O 1s spectra were fitted using the following compounds: iron oxide at 531.9 eV, FeO(OH) at 530.2 eV, CaO at 530.8 eV, and C=O/H_2O at 533.8 eV.

3 Results

3.1 STEM-EDS analysis of the deformed layers after wear

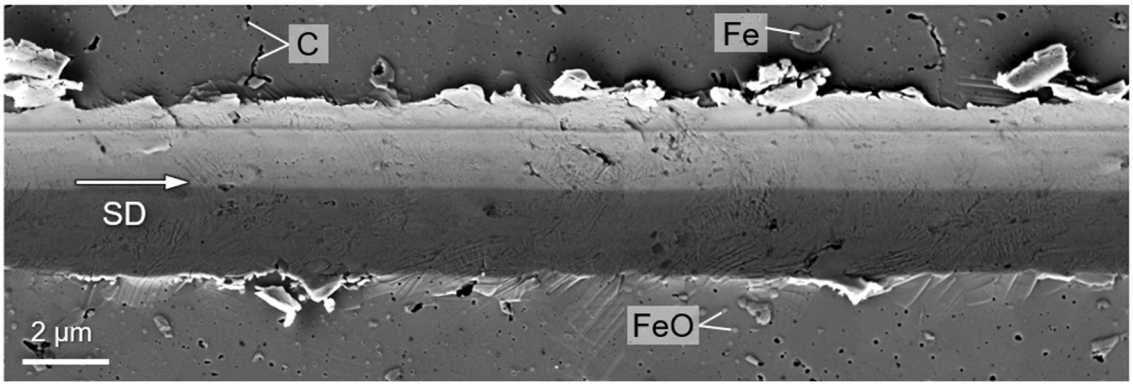

Fig. 1. SEM image of the cementite surface after the microscale sliding wear experiment (combination of two images). Due to sample fabrication, non-cementite inclusions (iron, graphite, and wüstite) exist, which are marked. The white arrow shows the sliding direction (SD).

Fig. 1 shows the wear track groove after the microscale sliding wear experiment. The sample is chemically inhomogeneous as it contains small fractions of iron (Fe), iron oxide (FeO, wüstite) according to XRD analysis, and remnant graphite after spark plasma sintering, as concluded based on the EDS measurements (section 2.1). Graphite is distributed in spherical and plate-like inclusions (black features in Fig. 1). The same black features are also assigned to the porosity that remains after the sample preparation. The remaining iron is located in relatively large grains that are similar to cementite. Small spherical particles consist of iron oxide FeO (light gray in Fig. 1). Inside the wear track groove, the non-cementite particles are difficult to distinguish, and the surface appears smooth.

We start the chemical investigation by examining the local elemental distribution in the wear-track cross-section via STEM-EDS (Fig. 2). The EDS results were obtained from the region investigated in the previous work where the Hägg carbides were observed. Below the contact surface (Fig. 2a), the microstructure is severely deformed and is divided into three distinct layers, as discussed in our previous investigation [21]: a nanocrystalline region right below the wear track, an ultra-fine-grained region, and a transition region towards the bulk virgin material. Table 1 summarizes the characteristic features of these layers, as described in [21].

Table 1. Characteristic features of microstructure below the contact surface

Region	Thickness (nm)	Grain size (nm)	Characteristic features
Nanocrystalline (NR)	200-300	~10	Nanoscale refinement, grain rotation, Hägg carbide formation
Ultra-fine-grained (UFGR)	250	~100-200	Fragmentation, grain boundary sliding
Transition (TR)	~ 1000	~500	Dislocation slip, shear band formation
Undeformed	-	~500	Low dislocation density

Apart from the cementite grains, we observe the finely dispersed graphite and iron oxide particles (light gray particles in Fig. 2a) in the ultra-fine-grained and transition regions. These particles are of similar size and are distinguished based on the EDS elemental mappings (Fig. 2c,d). While iron oxide inclusions are carbon-deficient compared to the surrounded cementite, graphite particles have an abundance of carbon (Fig. 2c). Graphite particles also contain some oxygen, as evident from Fig. 2d. The vertical carbon-depleted and iron-enriched regions are caused by FIB milling artifacts, i.e., curtaining, and are already visible in the bright-field STEM image (Fig. 2a). The EDS individual elemental mappings of iron, carbon and oxygen are in Appendix A (Fig. A8).

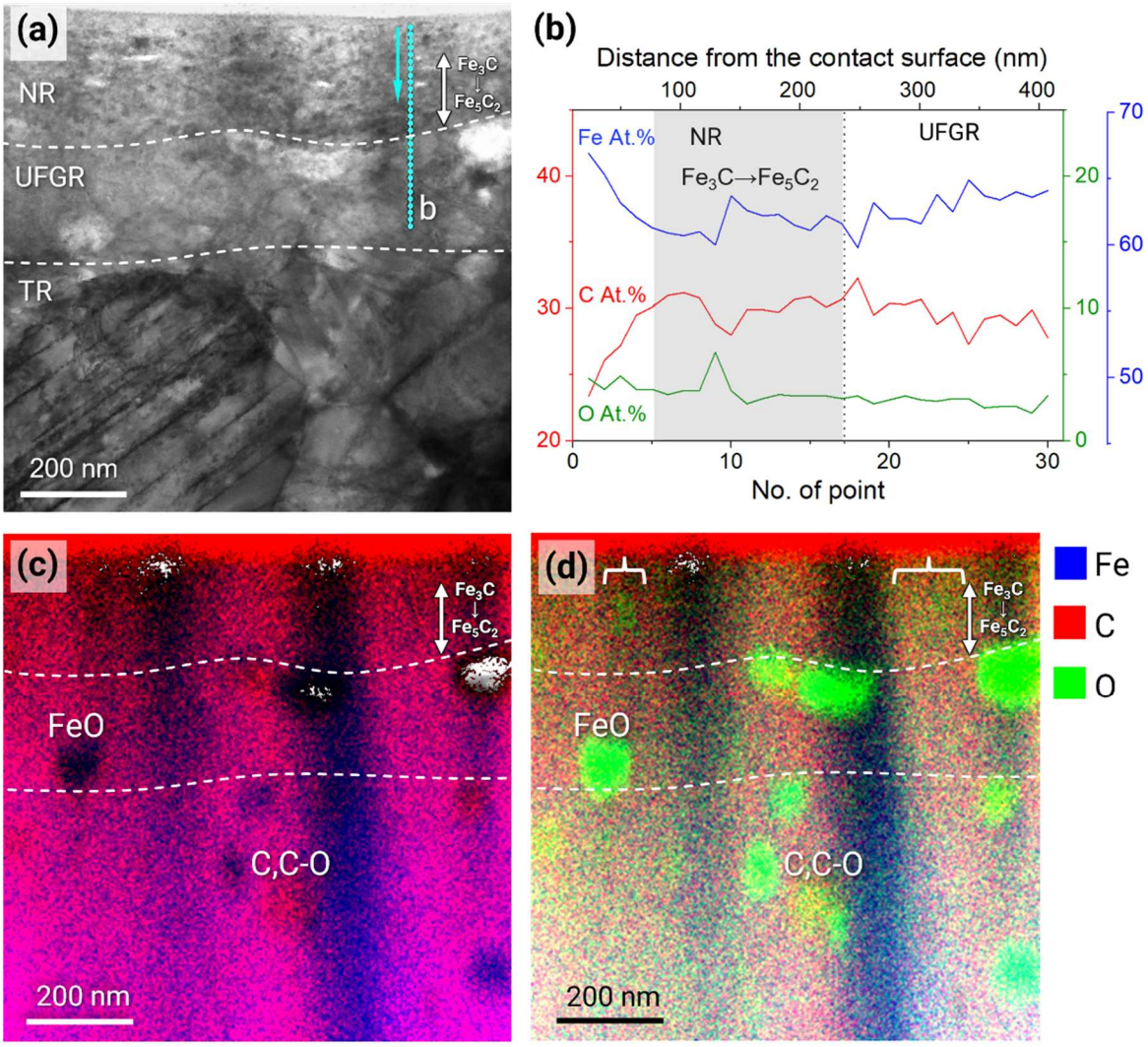

Fig. 2. STEM-EDS measurements of the wear track cross-section after a single-pass wear experiment. (a) STEM bright-field (BF) image of the wear track cross-section with the highlighted characteristic deformed regions [21]: nanocrystalline region (NR), ultra-fine-grained region (UFGR), transition region (TR). The cyan dotted line marks the location of the elemental profile in (b). (b) Elemental profile showing atomic concentrations of Fe, O, and C in the NR and UFGR. The gray rectangle marks the approximate depth range where Hägg carbides (Fe_5C_2) were detected. (c-d) EDS maps of the region displayed in (a). The horizontal white dashed lines indicate the approximate boundaries between NR, UFGR and TR according to the STEM-BF image. The two-sided white arrows in a,c,d mark the approximate depth range where the majority of Hägg carbide crystallites were detected. The white brackets in (d) mark the nanocrystalline region with increased C and O contents.

In the outermost nanocrystalline region, the elemental distribution is relatively homogeneous, and the individual non-cementite inclusions are barely visible, which is caused by deformation-driven decomposition due to the severe shear strains and high strain rates [21]. We also observe slightly higher oxygen and carbon concentrations in the nanocrystalline region compared to the other deformed regions (Fig 2c,d).

The relative differences in atomic concentrations are also evident from the line profile across the nanocrystalline and ultra-fine grain regions in Fig. 2b. This line profile was obtained from the same region where Hägg carbide (Fe_5C_2) formation was previously observed [21]. Right below the wear track (20-70 nm from the contact surface), the atomic fraction of iron is the highest (67 at.%) and decreases gradually with the increasing distance from the contact surface to 61 at.%. In the same depth range, the carbon concentration increases from 23 at.% to 31 at.%, while oxygen concentration decreases from 4.7 at.% to 3.5 at.%. As the distance from the contact surface increases further (70-240 nm), the atomic concentrations fluctuate around constant values (61.6 at.% Fe, 30.1 at.% C, and 3.7 at.% O) with the local changes not exceeding 4 at.%. These fluctuations indicate that the mechanical mixing in the nanocrystalline region did not result in a homogeneous elemental distribution. In the ultra-fine grain region, local fluctuations also occur. However, the overall trends of the atomic concentrations are changed. The atomic concentration of iron increases, whereas oxygen and carbon concentrations decrease. Another line profile across the nanocrystalline and ultra-fine grain region about 330 nm to the right from the profile on Fig. 2b was recorded, and that line confirms these local concentration trends (Fig. A9). In the undeformed cementite grains, the average atomic fractions of iron, carbon, and oxygen are measured as 76.4 at.%, 16.3 at.%, and 0.8 at.%, respectively. The comparison of the average atomic fractions from the nanocrystalline region and undeformed cementite grains confirms partial mechanical mixing due to severe shear deformation in the nanocrystalline region. Nonetheless, the measured atomic concentrations reported here do not represent the actual chemical compositions of the studied phases (section 2.3), and are discussed qualitatively in the following sections.

3.2 AES analysis of carbon bonding outside and inside in wear track

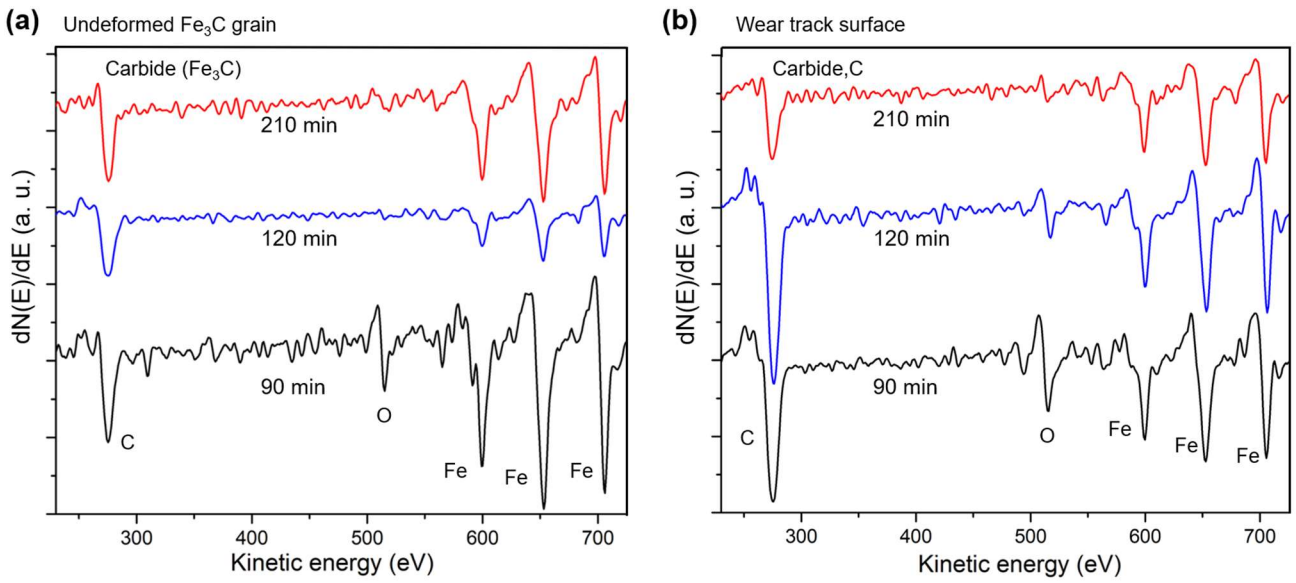

Fig. 3. Auger electron spectra acquired from the (a) undeformed cementite grain and (b) wear track surface at three increments of Ar^+ sputtering 90, 120, and 210 min. The positions of the carbon, oxygen, and iron peaks are marked.

Fig. 3 demonstrates the derivative Auger spectra obtained from the undeformed cementite grain and the wear track surface. According to the SEM images of the wear track surfaces before and after Ar^+ sputtering, the depth of the transition region (approx. 400 nm) was reached after 210 min (Fig. A5, Appendix A). The carbon spectra correspond to the KLL transitions and have distinctive shapes, depending on the chemical bonding [43–45]. The distinctive shape allows to distinguish between carbides (carbon-metal bonding) and graphite (carbon-carbon bonding). The carbon spectra recorded at the first two sputtering steps from the undeformed cementite grain (Fig. 3a) correspond to the combination of the two bonding types. This observation indicates the presence of carbides and graphite; the latter exists due to the remnant surface contamination or due to graphite particles in the region. After 210 min of sputtering, a typical carbon-metal bonding line-shape is revealed. Inside the wear track, all Auger spectra for carbon are composed of the two carbon line-shapes after all sputtering steps: this detail confirms the presence of graphite (in addition to carbides) in the deformed region. It is noteworthy that iron oxide and graphite are lighter components with lower binding energy and therefore are selectively etched compared to cementite during the sputtering process [46](Fig. A5). However, since the presence of graphitic carbon spectra inside the wear track is still evident during the entire sputtering sequence, we conclude that the results were not severely affected by the selective sputtering of lighter compounds.

3.3 XPS investigation of the phase composition

To investigate the phase composition in the deformed layers, we perform a comparative analysis of the XPS depth profiles in the undeformed cementite as well as in the wear array area. Fig. 5 presents the Fe 2p3/2 and C 1s spectra obtained after one of the initial sputtering steps (126s, 70 nm depth). At this sputtering step, the component peaks are a combination of the surface contamination layer and the sample bulk.

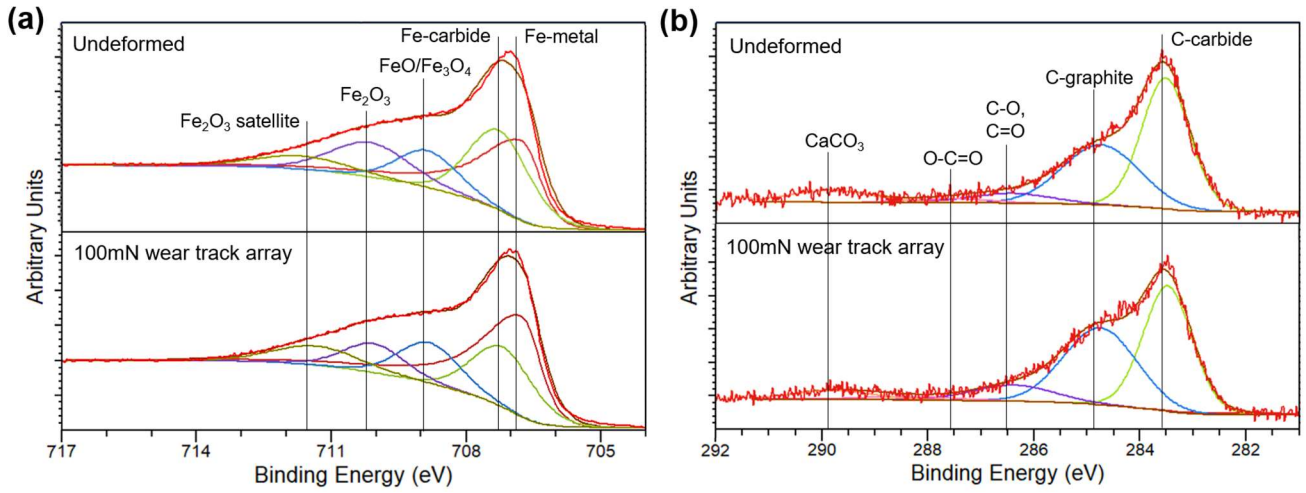

Fig. 5. XPS spectra recorded after 126 s of sputtering (~70 nm depth) from the undeformed cementite and the wear track array. (a) Fe 2p3/2 spectra with deconvoluted Fe-metal, Fe-carbide, Fe_3O_4/FeO, Fe_2O_3, and Fe_2O_3-satellite peaks. (b) C 1s spectra with deconvoluted C-carbide, C-graphite, C-O, C=O, O-C=O, and $CaCO_3$ peaks.

The Fe 2p3/2 spectra are composed of five peaks (Fig. 5a): Fe-metal, Fe-carbide, Fe_3O_4/FeO, Fe_2O_3, and Fe_2O_3-satellite. Due to the oxidation of the metallic iron and FeO in the atmosphere, additional peaks of Fe_2O_3 and Fe_2O_3-satellite are expected. Since the difference between the binding energies of the overlapping Fe-metal and Fe-carbide is small (~0.4 eV), the spectra decomposition leads to ambiguous results at ~707 eV. Therefore, we refer to the sum of the Fe-metal and Fe-carbide concentrations in the quantitative phase analysis. We deconvoluted the C 1s spectra using the following compounds: C-carbide (cementite, Hägg carbide), C-graphite, C-O, C=O, O-C=O, and $CaCO_3$ peaks. While $CaCO_3$ is a component of the surface contamination layer, C-graphite, C-O, C=O and O-C=O are also present in the bulk sample, as was evident from the previously discussed EDS observations (Fig. 2d). The difference in the binding energies between the C-carbide C-graphite is rather large (~1.4 eV), allowing for the adequate quantification of the individual fractions. For convenience, we refer to the sum of the C-O, C=O, O-C=O, and $CaCO_3$ fractions as other C-compounds during phase composition analysis.

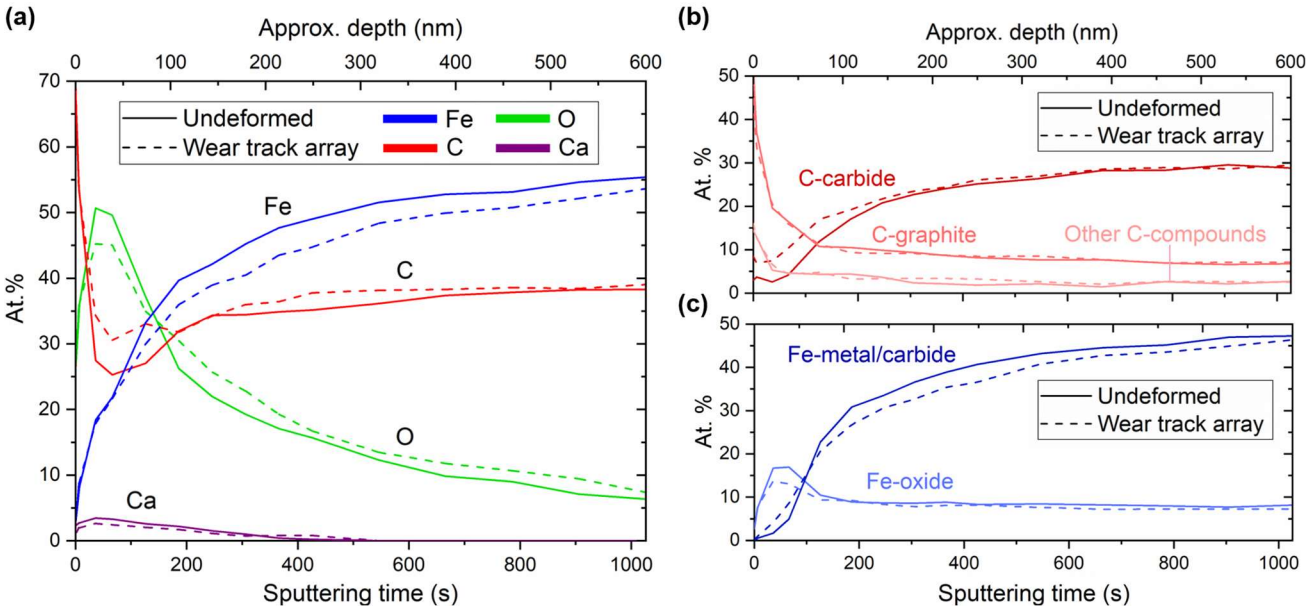

Fig. 6. (a) XPS depth profiles for undeformed cementite and wear track array. (b) C-carbide, C-graphite, and other C-compounds at.% fractions throughout XPS depth profile (c) Fe-metal/carbide and Fe-oxide at.% fractions throughout XPS depth profile.

The XPS elemental depth profiles (Fig. 6a) show similar trends for undeformed cementite and deformed wear track arrays. With extended sputtering periods and higher depth, the surface contamination is gradually removed, revealing the composition below the surface. The atomic concentration of iron rapidly increases until 300 s (175 nm) but does not demonstrate a drastic change after further sputtering, increasing gradually by an additional 10 at.%. The fraction of carbon is initially high (70 at.%) due to surface contamination, which is dissociated during the first two sputtering periods between 0 s and 36 s (0-21 nm). At the higher sputtering depth at 36-126 s (21-74 nm), there is a drop in C at.%, followed by a further increase to a constant value of ~38 at.%. The oxygen concentration initially increases from ~26 at.% at the surface to more than 45 at.% at 36-66 s (21-39 nm) and then gradually decreases to less than 8 at.% at the end of sputtering. The gradual decrease of oxygen content is related to the presence of plate-like pores that can exceed 1 μm in length (Fig. 1) and affect the measured composition throughout the entire measured depth profile (0-600 nm). The overall carbon and oxygen trends imply that the top contamination layer (0-36 s, 0-21 nm) is mainly formed by the carbon/oxygen-saturated compounds, whereas a film of iron oxide mixtures exists at higher depths. A tiny calcium fraction is detected up to ~500 s (290 nm) and is associated with Ca_2C, $CaCO_3$, CaO, and $Ca(OH)_2$ compounds [35]. Calcium might originate from the surface preparation slurry and reside in sample pores at the surface.

There are, however, several discrepancies when comparing the depth profiles from the undeformed and the wear track region (Fig. 6a). On the one hand, the iron concentrations are nearly the same for the undeformed and deformed regions during the first sputtering steps. On the other hand, starting from 126 s (74 nm), the iron fraction in the deformed region is consistently 3.3 at.% lower than that in the undeformed region. Additionally, the oxygen concentrations show an opposite trend: in the 6-126s range (3.5-74 nm), the O at.% is up to 5.5 at% lower in the wear track array, whereas it is higher than the O fraction in the undeformed region by ~2.3 at.% at all subsequent sputtering steps. The carbon concentrations are also higher in the deformed case, with the highest difference of ~6 at.% between 36 and 126s (21-74 nm). Although the calcium fraction is smaller in the wear track array region, it can still be detected after a bit longer sputtering in the deformed region than in the undeformed region.

By comparing the atomic fractions of carbon and iron assigned to specific compounds, we examine the phase composition differences in more detail (Fig. 6b, c). After the initial maximum at the surface level, C-graphite rapidly decreases and does not significantly change after 126 s (74 nm, Fig. 6b). The C at.% in graphitic carbon is similar in both regions through the entire depth profile (Fig. 6b), except for the initial sputtering steps, after which C-graphite is smaller in the deformed region (max. difference ~13 at.% at 66 s). The same is true for the carbon in other compounds (Ca_2C, C-O, C=O, O-C=O, and $CaCO_3$), whereas the maximum difference does not exceed 2 at.%. On the contrary, the C at.% in the carbide phase is consistently higher in the wear track array up to 246 s (144 nm). The C-carbide fraction significantly increases between 36 and 246s (21-144 nm) and continues to increase slowly with further sputtering (Fig. 6b). The Fe-metal/carbide and Fe-oxide fractions are generally smaller in the wear track array, with the exception of Fe-metal/carbide concentration being slightly higher in the deformed region up to 66 s (39 nm, Fig. 6c). The initial Fe-oxide peak reaches its maximum at 36-66 s (21-39 nm) and then decreases to a nearly constant level at ~126 s (74 nm). These observations lead to a conclusion that most of the surface contamination (iron oxides, calcium, and carbon compounds) is eliminated

after 126 s (74 nm) of sputtering, and the rest of the contamination in larger plate-like pores has a less pronounced effect on the measured composition and gradually decreases by the end of the sputtering sequence.

4 Discussion

4.1 Elemental and phase distribution after wear

Due to tribological loading, the non-cementite inclusions (iron, graphite, and wüstite) in the most severely deformed regions undergo decomposition and mechanical mixing with the cementite matrix, as evident from the EDS observations (Fig. 2). As previously observed [21], the intense localized strains in the nanocrystalline region lead to severe plastic deformation and grain refinement, which resembles the formation of a shear band and promotes the mechanical mixing of phases by shear transfer [47]. However, the fluctuations on the EDS line profiles (Fig. 2b, Fig. 9b) indicate that deformation due to single-pass wear is not sufficient to cause the complete homogenization because local gradients in iron, carbon, and oxygen concentrations still exist. Please note, however, that single-pass wear is sufficient for the formation of Hägg carbides (Fe_5C_2), as proven previously by selected electron diffraction [21].

Due to the mechanical mixing in the nanocrystalline and ultra-fine-grained regions, the elemental distribution in these regions is very different from the bulk cementite. We also observe a more homogenized elemental composition in the nanocrystalline region in EDS. In contrast, the elemental distribution in the ultra-fine-grained region gradually transitions towards the atomic concentrations in the bulk cementite (Fig. 2b, Fig. A9b). According to the EDS results, right below the contact surface (0-70 nm depth), the iron fraction is high (Fig. 2b, Fig. A9b), which does not align with the present XPS measurements (Fig. 6a). Since the local changes from a large region with a 100 µm diameter are averaged in the XPS results, we presume that the iron increase below the contact surface is attributed to the presence of an iron grain near the surface in the EDS image. In addition, according to the XPS measurements, the outermost ~74 nm are the most affected by the iron oxide formation and presence of contamination compounds.

The depth profiling in XPS reveals similar trends in elemental distribution for the undeformed and deformed regions. However, the carbon and oxygen fractions are higher in the deformed region than in the undeformed region after the first sputtering steps, and calcium is detected after longer sputtering periods. This finding is potentially related to the intermixing of the surface contamination layer and non-cementite precipitates containing carbon, oxygen, and calcium compounds with the bulk material or storage of calcium compounds in large plate-like pores. Another possible explanation of higher C and O fractions in the deformed region is that the measurement of the elemental distribution by XPS is partially affected by the wear-induced surface roughness that potentially prevents the uniform sputtering. Nonetheless, a substantial amount of the other carbon compounds (Ca_2C, C-O, C=O, O-C=O, and $CaCO_3$) is removed by 126 s of sputtering (74 nm).

4.2 Analysis of carbon sources for Hägg carbide (Fe_5C_2) formation

Our previous work confirmed the formation of the Hägg carbide (Fe_5C_2) at the expense of cementite in the nanocrystalline region [21]. Two mechanisms of excess carbon formation were proposed that provide the driving force for phase transformation. One way of promoting the local carbon enrichment arises from the decomposition of non-cementite inclusions that remain after sintering, i.e., the dissolution of finely dispersed graphite particles. Another scenario is based on cementite tribo-oxidation, accompanied by the loss of iron and the simultaneous relative increase in carbon, which then is available for transformation. According to the

previous APT measurements, a higher fraction of carbon-saturated regions and a higher oxygen content are found in the nanocrystalline region compared to the undeformed cementite grain. Nonetheless, the average C/Fe ratio was nearly the same in both cases. Other carbon compounds (Ca_2C, C-O, C=O, O-C=O, and $CaCO_3$) can also potentially act as a source of excess carbon for the transformation. However, these compounds are mostly found within the top 70 nm (Fig. 6b), above the region where Hägg carbide formation was previously observed. At the greater depths, other carbon compounds are stored in the large, far-scattered plate-like pores, and their fraction is significantly smaller than the fraction of graphite. Therefore, their effect on the phase transformation in the 70-240 nm depth range is unlikely.

The EDS results from the same region and depth range in which Hägg carbides (Fe_5C_2) were detected previously (70-240 nm) demonstrate local fluctuations consistent with the formation of carbon-saturated regions in APT. The average carbon and oxygen content was higher in the deformed than in the undeformed area. Moreover, the carbon fraction remains as high in the outer part of the ultra-fine-grained region as in the nanocrystalline region. However, since the phase transformation is only observed in the nanocrystalline region and not in the ultra-fine-grained region [21], the high carbon concentration is not the only requirement for the Hägg carbide formation.

The second requirement for the Hägg carbide formation is severe plastic deformation in the nanocrystalline region, which leads to nanoscale refinement and high defect density. The associated formation of new interfaces gives rise to the free energy, thus allowing for the Hägg carbide formation. In the ultra-fine-grained region, the shear strains are not as severe as in the nanocrystalline region, the saturation grain size after fragmentation is significantly larger (Table 1). In addition, the transformation of cementite into the Hägg carbide is often explained through the model of chemical twinning since the crystal structures of both phases can be described as layers of trigonal prisms, and the arrangement of the prisms defines the forming phase [48]. This model emphasizes the crucial role of severe shear strain and the higher likelihood that cementite-Hägg carbide transformation was displacive by straining the cementite lattice and its subsequent shearing during wear.

The formation of new interfaces and potential rapid frictional temperature increase in the contact zone could also assist carbon-diffusion. Long-range carbon diffusion would be essential for Hägg carbide crystallization from the non-equilibrium amorphous Fe-C mixture [49,50]. In contrast, in this study, Hägg carbides formed already after the single-pass wear experiment which does not result in massive frictional temperature increase and its duration is too limited for long-range diffusion.

The analysis of the cementite-Hägg carbide transformation based on XPS data is complicated because both phases have the same bonding and, consequently, the same binding energy of carbon in both carbides. Additionally, small differences between the binding energies of Fe-metal and Fe-carbide (section 2.3) are an obstacle to clear peak separation. Nonetheless, the comparison of carbon fractions assigned to the carbide phase (Fig. 6b) demonstrates a substantial increase in the C-carbide concentration in the wear track array up to 246 s (144 nm). The average difference is 4.5 at.% at 0s-186s (0-109 nm) and corresponds to the expected difference between stoichiometric cementite and Hägg carbide (3.6-6.25 at.%).

To better examine the possible carbon sources of Hägg carbide (Fe5C2) formation, we analyze the ratios of C-graphite and C-carbide fractions as well as Fe-oxide and Fe-metal/carbide fractions (Fig. 7) in those regions in which a higher C-carbide concentration was observed in the wear track array (Fig. 6b). We plot the corresponding ratios for the undeformed region and compare them to those in the wear track array. Although

the ratios are affected by the surface contamination during the first sputtering steps (up to 126s, 74nm), their overall trends reveal the excess carbon source (Fig. 7).

The decomposition of the remaining graphitic carbon in the sample would lead to a lower C-graphite content and a higher C-carbide fraction. As such, a C-graphite/C-carbide ratio would be lower in the deformed region than in the undeformed region. This evolution is indeed observed: the ratios of C-graphite and C-carbide fractions are lower for the wear track array. Although the decrease of C-graphite/C-carbide in the wear track array is also partially due to the removal of the surface carbon layer (until 126s, 74 nm), the deviation between the carbon ratio curves remains until 186s (109 nm), whereas the iron ratios coincide already after 126s (74 nm). Therefore, we assume that the lower ratios of C-graphite and C-carbide fractions are attributed to the formation of carbidic bonds of Hägg carbide and the simultaneous decrease of graphitic carbon bonds in the deformed region. Thus, the graphite decomposition resulting in carbon oversaturation and Hägg carbide formation is supported by the XPS measurements. Nonetheless, the presence of iron carbides and graphite in the deformed region indicates that the released carbon from graphite did not fully transform (see AES and XPS measurements).

The other source of carbon excess would be the tribooxidation of cementite. In this case, the Fe-oxide fraction would increase, whereas the Fe-metal/carbide fraction would simultaneously decrease. This iron redistribution would lead to a higher ratio between Fe-oxide and Fe-metal/carbide in the wear track compared to the undeformed region. This evolution is not observed in the present experiments. According to Fig. 7, the ratio between Fe-oxide and Fe-metal/carbide is lower in the deformed case, which indicates the removal of the surface iron oxide layer and not the formation of more iron-oxygen bonds.

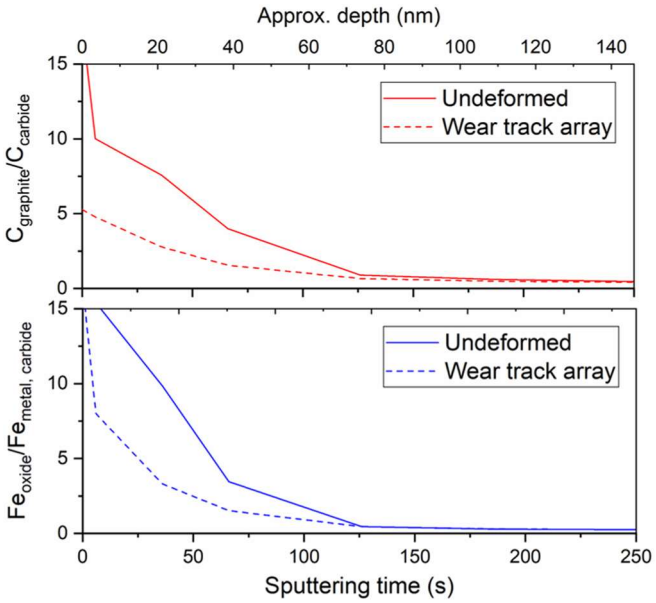

Fig. 7. The ratios of atomic concentrations in (a) carbon and (b) iron compounds in undeformed cementite and wear track array.

The observed cementite-Hägg carbide transformation in the outermost deformed layer due to the presence of graphitic carbon is not limited to sintered bulk cementite with remaining graphite as it can take place in graphite-rich cast iron. For instance, the transformation might occur in graphite cast iron employed in brake discs and diesel engine components that are often subjected to wear [51–53]. Due to the tribological loading

on lamellar, compacted, or spheroidal graphite cast iron, graphite tends to abrade and form a low-friction film that is further deformed – along with the pearlite matrix – during the following wear cycles. On the one hand, this process introduces carbon gradients into the material, similarly to the cementite-Hägg carbide transformation conditions during iron powder ball milling in a high-carbon medium [26,27] or iron carburization [28]. On the other hand, the presence of ferrite could also cause cementite decomposition, as ferrite and graphite would form a stable equilibrium mixture in such a material [54–56].

The wear-induced chemical changes are strongly interlinked with the changes in tribological properties. In the work of Kobs et al. [57], the wear behavior of 52100 bearing steel was investigated after carbon ion implantation. Upon implantation, significant friction and wear reduction were reported due to the formation of the surface layer of intermediate hexagonal ε-carbide ($Fe_{2.4}C$) and pure carbon. The subsequent annealing at 500°C led to the transformation of ε-carbide into Hägg carbide (Fe_5C_2), drastically reducing the wear resistance [57]. In the later study by Wilbur and Buchholtz [58], the carbon ion implantation on the α-Fe disc at different temperatures caused the formation of ε-carbide, Hägg carbide, and cementite, all of which had better tribological performance than the unimplanted iron. The wear resistance of the metal with Hägg carbides was better than that with ε-carbide, and cementite has demonstrated as having the best tribological behavior among all studied iron carbides [58]. These studies show that cementite-Hägg carbide transformation may worsen the wear response and is undesirable for cementite-strengthened steels.

5 Conclusion

The surface spectroscopy measurements of sample composition before and after microscale wear experiments on polycrystalline cementite with minor fractions of iron, graphite, and wüstite reveal chemical changes due to tribological loading. The following conclusions are drawn from this study:

- Severe plastic deformation during tribological loading induces decomposition of non-cementite particles and subsequent mechanical mixing with the cementite matrix by shear transfer. The mechanical mixing is especially pronounced in the outermost deformed region (nanocrystalline region); however, it does not lead to a fully homogeneous elemental distribution. Mechanical mixing is not pronounced in the lower deformed regions, although the non-cementite particles are deformed.
- Although the elemental distribution in the deformed region may differ locally, the average atomic concentrations in the undeformed and deformed regions are similar. In the region covered by a wear track array, the carbon and oxygen surface contamination and iron oxide layer are partially removed and mixed with the bulk material compared to the undeformed region.
- The previously observed cementite-Hägg carbide transformation occurs in the region with an increased fraction of carbon. Comparing the iron and carbon compounds ratios reveals that graphite decomposition is responsible for the excess carbon formation in the nanocrystalline region. On the other hand, the effect of cementite oxidation on Hägg carbide formation is negligible.

Acknowledgements

The authors thank Y. Todaka of the Toyohashi University of Technology for providing cementite samples. We would also like to thank R. Kircheim, D. Ponge, and M. Herbig for the fruitful discussions. The authors thank U. Hagemann of the University of Duisburg-Essen for conducting AES measurements. H. T. acknowledges her Ph.D. fellowship from the International Max Planck Research School for Surface and Interface Engineering (IMPRS-SurMat).

Appendix A. Supplementary material

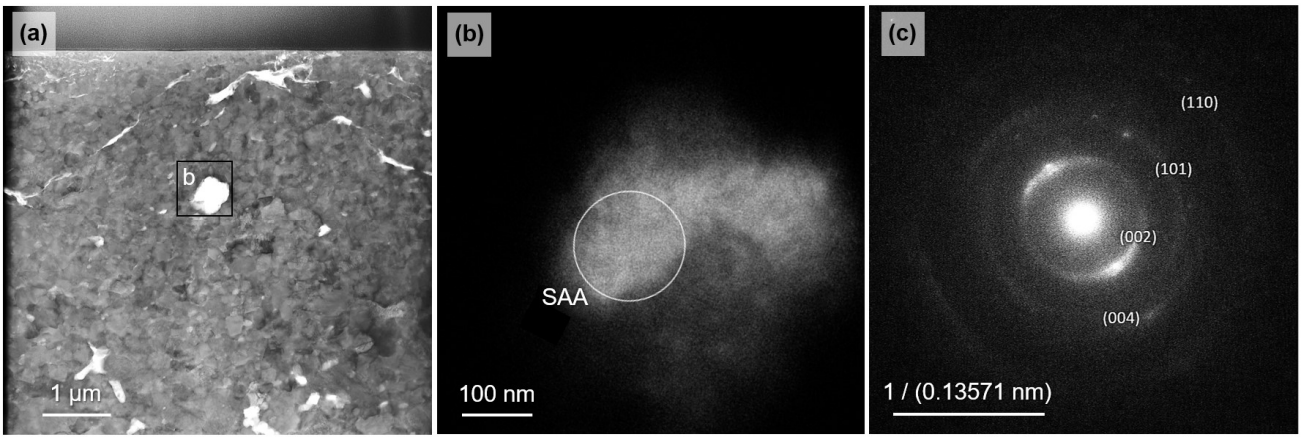

Fig. A1. (a) STEM BF image of polycrystalline cementite sample showing a graphite particle in (b). (c) Diffraction pattern showing graphitic reflections. These results implicate that the carbon is indeed graphite and not glassy carbon.

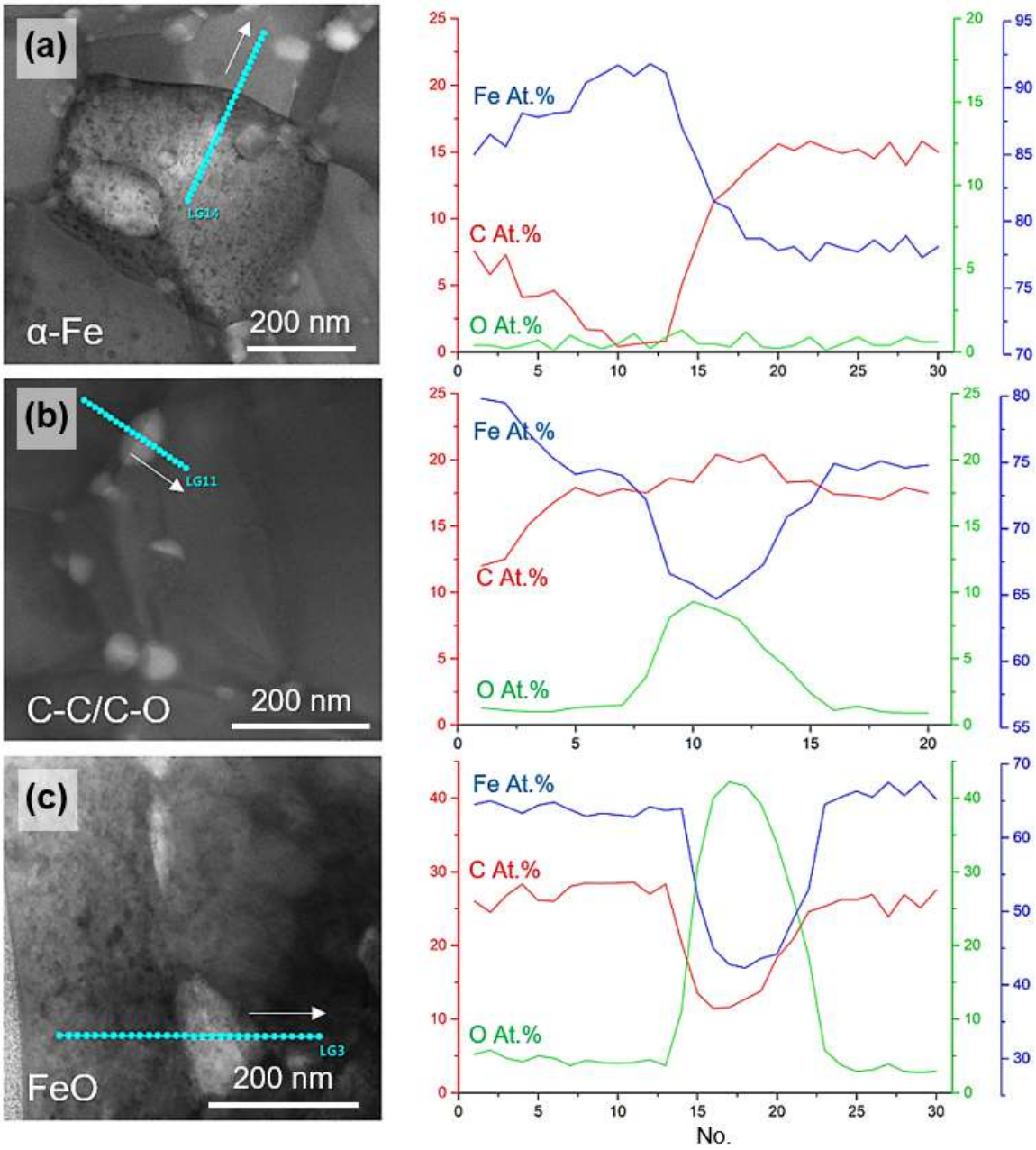

Fig. A2. EDS composition measurements of non-cementite particles in the sintered polycrystalline sample: (a) iron, (b) graphite, and (c) iron oxide. White arrows mark the sequence of data acquisition.

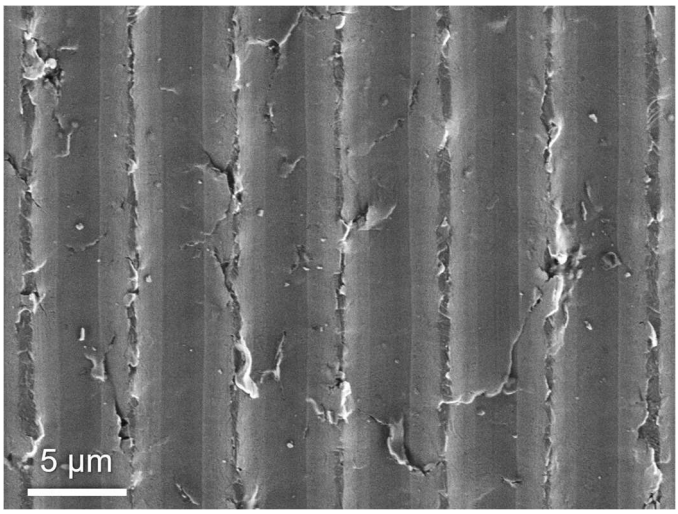

Fig. A3. SEM image of the 800 x 800 µm wear track array fragment, demonstrating ~92% coverage of the surface with wear track grooves.

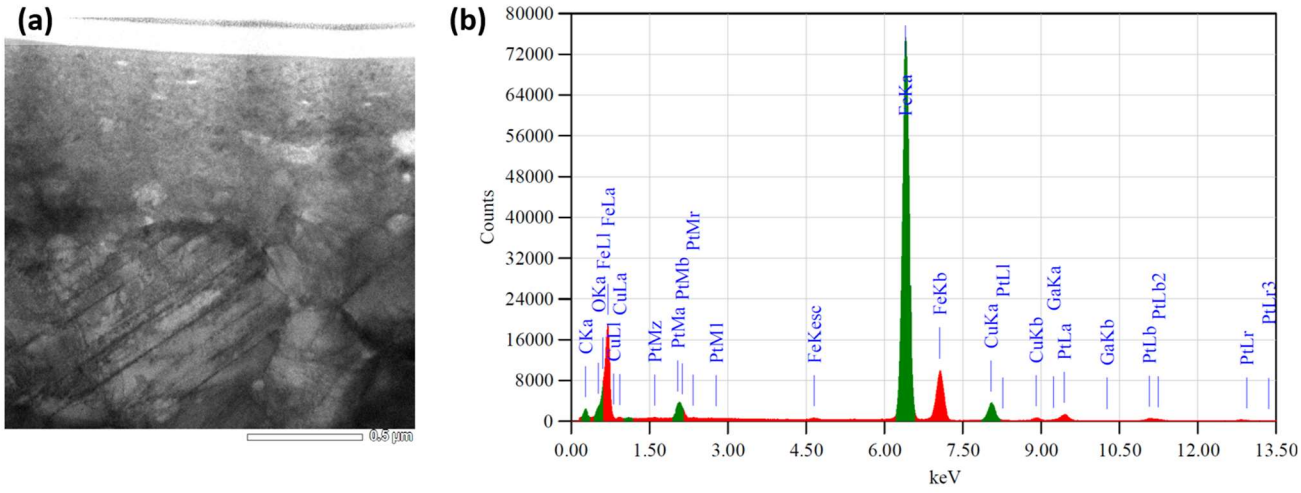

Fig. A4. The region below the wear track and (b) the corresponding EDS spectrum with marked detected peaks.

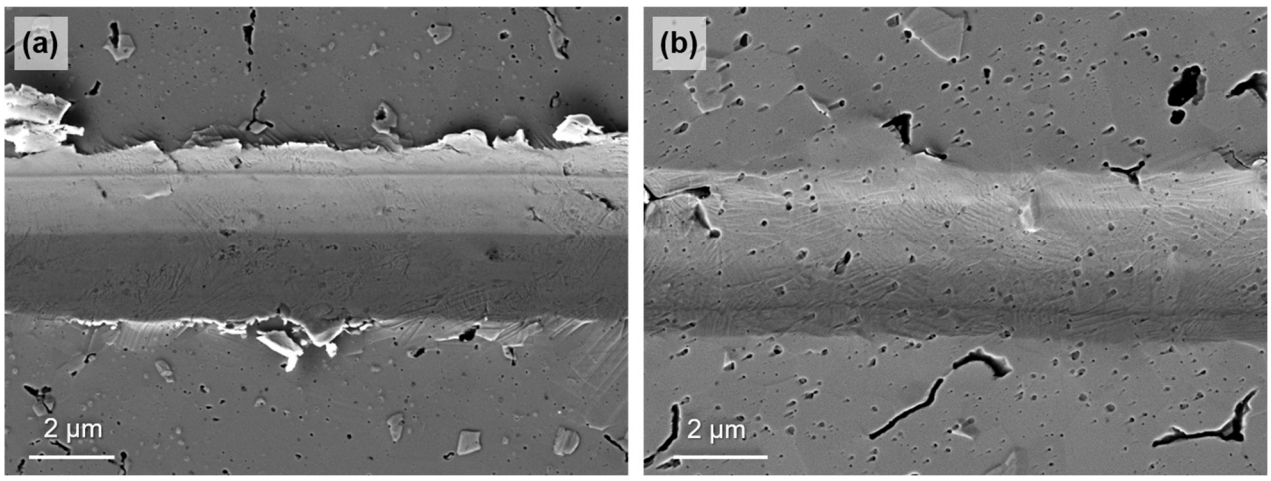

Fig. A5. SEM images from (a) non-sputtered wear track surface and (b) wear track surface after the 210 min of Ar^+ sputtering revealing preferential etching of iron oxide and graphite particles compared to the cementite. After sputtering the wear track surface, slip traces from TR become visible.

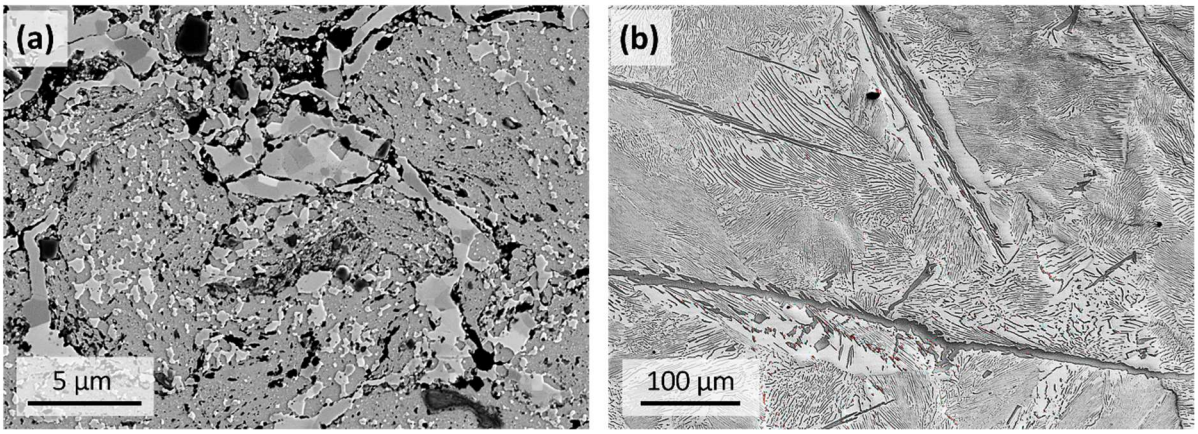

Fig. A6. SEM images of two samples used for calibrating parameters for XPS peaks deconvolution: (a) sintered sample with graphite (black inclusions) and cementite (large polycrystalline gray inclusions) in the α-Fe matrix; (b) hypereutectoid pearlitic steel.

To increase the accuracy of chemical composition quantification by XPS, additional spectra from two samples (Fig. A6) were recorded after 600s of Ar^+ sputtering for the calibration of the peak fitting parameters. One of the calibration samples (Fig. A6a) was prepared by spark plasma sintering of mechanically alloyed Fe and C powders and contained large fractions of graphite and cementite in the α-Fe matrix. The presence of graphite and cementite in large quantities allowed for the optimization of their peak shapes and positions when deconvoluting the C 1s spectra since both peaks were well pronounced. The binding energies of graphitic C and carbidic C initially used for the curve fitting were ~284.5 and ~283.3 eV, respectively, which led to the residual standard deviation of 1.5-2 arb. unit with respect to experimentally obtained spectra (Fig. A7a). After using optimized values of ~284.9 eV and ~283.5 eV for the graphitic and carbidic peaks (Fig. A7b), the residual standard deviation was decreased to about 1.1-1.2 arb. unit. The second calibration sample (Fig. A6b) is hypereutectoid pearlitic steel prepared by the standard heat treatment procedure with a composition of 1.15 wt.% C (5.15 at.% C, 94.85 at.% Fe). The parameters were hence optimized to ensure that the measured C at.% to Fe at.% ratio was close to the calculated ratio of 0.054. The measured composition of the second calibration sample (Fig. A6b) was 6.27 at.% O, 5.58 at.% C and 88.14 at.% Fe (C at.% to Fe at.% ratio of 0.063) and validated the overall composition measurement and peak analysis. The analysis also shows that a slight overestimation of C fractions and an underestimation of Fe fractions by about 7% are possible. Fig. A7a compares curve fitting for the polycrystalline cementite sample before and after optimizing peak parameters with two calibration samples.

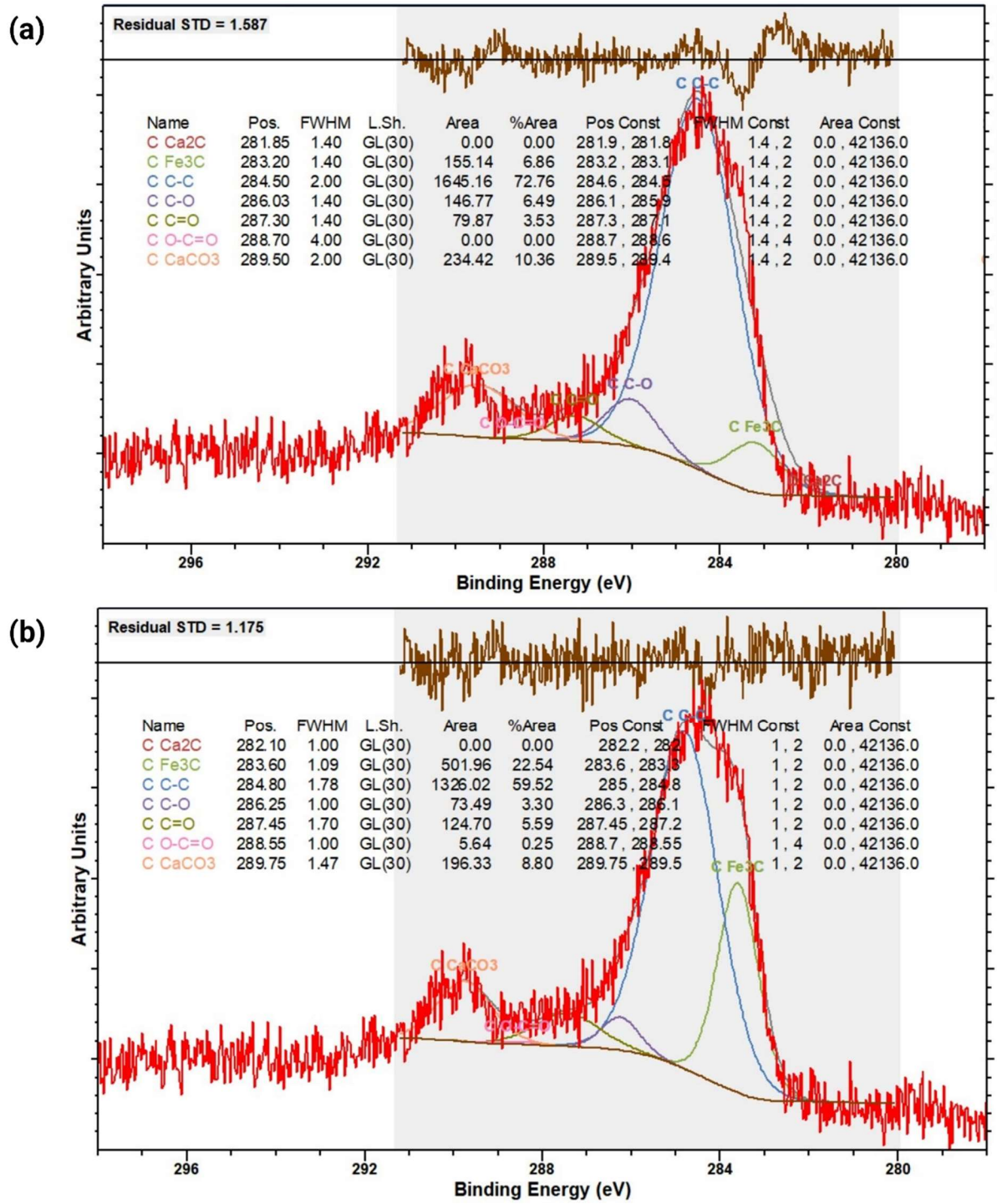

Fig. A7. Curve fitting in CasaXPS 2.3.22 software for the C 1s XPS spectra obtained from the undeformed region of polycrystalline cementite: (a) before and (b) after peak parameter optimization.

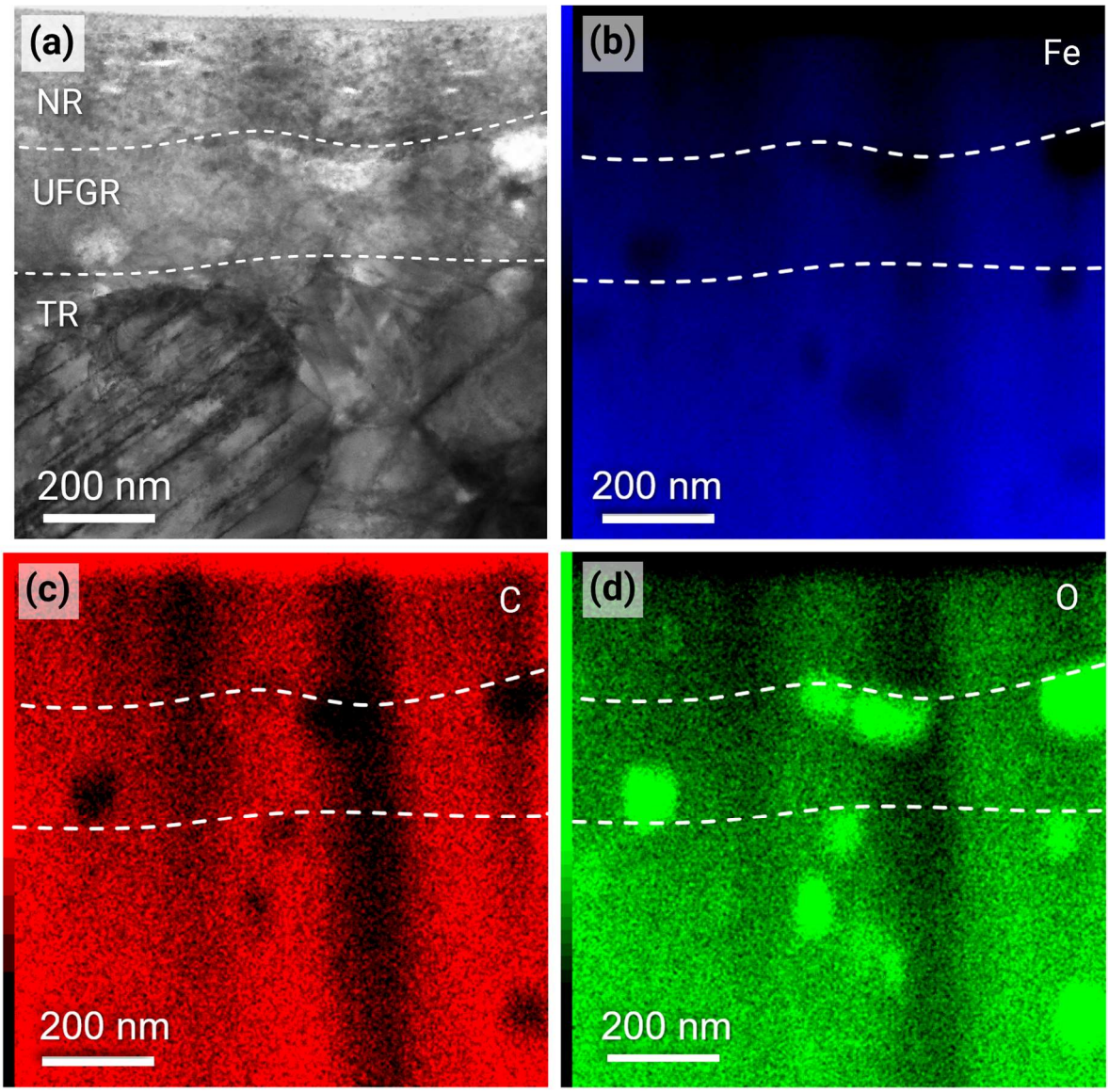

Fig. A8. STEM-EDS measurements of the wear track cross-section. (a) STEM bright-field (BF) image of the wear track cross-section after a single-pass experiment with marked characteristic deformed regions [21]: nanocrystalline region (NR), ultra-fine-grained region (UFGR), transition region (TR). EDS maps for (b) Fe, (c) C and (d) O of the region displayed in (a). The vertical carbon-depleted and iron-enriched regions are caused by FIB milling artifacts, i.e., curtaining, and are already visible in the bright-field STEM image (a). The horizontal white dashed lines indicate the approximate boundaries between the NR, UFGR and TR regions according to the STEM-BF image in (a).

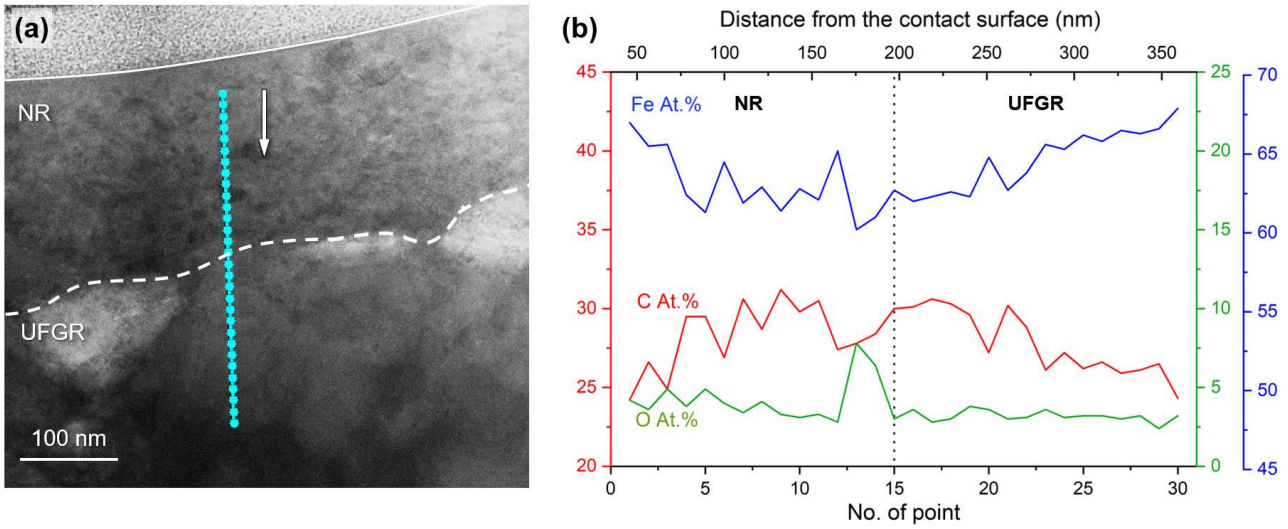

Fig. A9. EDS measurements of the wear track cross-section. (a) STEM bright-field (BF) image of the wear track cross-section after a single-pass experiment with marked characteristic deformed regions [21]: nanocrystalline region (NR) and ultra-fine-grained region (UFGR). The Blue dotted line marks the location of the elemental profile line in (b). (b) Elemental profile line showing atomic concentrations of iron, oxygen, and carbon. The dotted line highlights the approximate boundary between the nanocrystalline region (NR) and the ultra-fine-grained region (UFGR).

References

[1] B. Narayanaswamy, A. Ghaderi, P. Hodgson, P. Cizek, Q. Chao, M. Safi, H. Beladi, Abrasive Wear Resistance of Ferrous Microstructures with Similar Bulk Hardness Levels Evaluated by a Scratch-Tester Method, Metall. and Mat. Trans. A 50 (2019) 4839–4850.

[2] K. Mishra, A. Pachauri, A. Singh, Deformation, Wear and Microstructural Evolution of Nano-structured Pearlite Under Repeated Contact Sliding, Tribol. Lett. 66 (2018) 365.

[3] M.W. Kapp, A. Hohenwarter, S. Wurster, B. Yang, R. Pippan, Anisotropic deformation characteristics of an ultrafine- and nanolamellar pearlitic steel, Acta Mater. 106 (2016) 239–248.

[4] A. Bachmaier, R. Pippan, O. Renk, Effect of Carbon in Severe Plastically Deformed Metals, Adv. Eng. Mater. 22 (2020) 2000879.

[5] C. Borchers, R. Kirchheim, Cold-drawn pearlitic steel wires, Prog. Mater. Sci. 82 (2016) 405–444.

[6] G. Langford, Deformation of pearlite, Metall. Trans. A 8 (1977) 861–875.

[7] J. Embury, R. Fisher, The structure and properties of drawn pearlite, Acta Metall. 14 (1966) 147–159.

[8] J. Pan, L. Chen, C. Liu, G. Zhang, R. Ren, Relationship Between the Microstructural Evolution and Wear Behavior of U71Mn Rail Steel, J. Mater. Eng. Perform 30 (2021) 1090–1098.

[9] Y. Qin, D. Mayweg, P.-Y. Tung, R. Pippan, M. Herbig, Mechanism of cementite decomposition in 100Cr6 bearing steels during high pressure torsion, Acta Mater. 201 (2020) 79–93.

[10] J. Takahashi, M. Kosaka, K. Kawakami, T. Tarui, Change in carbon state by low-temperature aging in heavily drawn pearlitic steel wires, Acta Mater. 60 (2012) 387–395.

[11] Y.J. Li, P. Choi, S. Goto, C. Borchers, D. Raabe, R. Kirchheim, Evolution of strength and microstructure during annealing of heavily cold-drawn 6.3GPa hypereutectoid pearlitic steel wire, Acta Mater. 60 (2012) 4005–4016.

[12] J. Park, S.-D. Kim, S.-P. Hong, S.-I. Baik, D.-S. Ko, C.Y. Lee, D.-L. Lee et al., Quantitative measurement of cementite dissociation in drawn pearlitic steel, Mater. Sci. Eng. A 528 (2011) 4947–4952.
[13] F. Wetscher, R. Pippan, S. Sturm, F. Kauffmann, C. Scheu, G. Dehm, TEM investigations of the structural evolution in a pearlitic steel deformed by high-pressure torsion, Metall. and Mat. Trans. A 37 (2006) 1963–1968.
[14] S. Djaziri, Y. Li, G.A. Nematollahi, B. Grabowski, S. Goto, C. Kirchlechner, A. Kostka et al., Deformation-Induced Martensite: A New Paradigm for Exceptional Steels, Adv. Mater 28 (2016) 7753–7757.
[15] D. Mayweg, L. Morsdorf, X. Wu, M. Herbig, The role of carbon in the white etching crack phenomenon in bearing steels, Acta Mater. 203 (2021) 116480.
[16] A. Greco, S. Sheng, J. Keller, A. Erdemir, Material wear and fatigue in wind turbine Systems, Wear 302 (2013) 1583–1591.
[17] A. Kumar, G. Agarwal, R. Petrov, S. Goto, J. Sietsma, M. Herbig, Microstructural evolution of white and brown etching layers in pearlitic rail steels, Acta Mater. 171 (2019) 48–64.
[18] H. Chen, C. Zhang, W. Liu, Q. Li, H. Chen, Z. Yang, Y. Weng, Microstructure evolution of a hypereutectoid pearlite steel under rolling-sliding contact loading, Mater. Sci. Eng. A 655 (2016) 50–59.
[19] M. Umemoto, Z.G. Liu, H. Takaoka, M. Sawakami, K. Tsuchiya, K. Masuyama, Production of bulk cementite and its characterization, Metall. Trans. A 32 (2001) 2127–2131.
[20] T. Sasaki, T. Yakou, M. Umemoto, Y. Todaka, Two-body abrasive wear property of cementite, Wear 260 (2006) 1090–1095.
[21] H. Tsybenko, C. Tian, J. Rau, B. Breitbach, P. Schreiber, C. Greiner, G. Dehm et al., Deformation and phase transformation in polycrystalline cementite (Fe3C) during single- and multi-pass sliding wear, Acta Materialia (2022) 117694.
[22] M. Dirand, L. Afqir, Identification structurale precise des carbures precipites dans les aciers faiblement allies aux divers stades du revenu, mecanismes de precipitation, Acta Metall. 31 (1983) 1089–1107.
[23] H.K.D.H. Bhadeshia, Theory of transformations in steels, CRC Press, Boca Raton, 2021.
[24] G. Ghosh, G.B. Olson, Precipitation of paraequilibrium cementite: Experiments, and thermodynamic and kinetic modeling, Acta Mater. 50 (2002) 2099–2119.
[25] Y. Nakamura, T. Mikami, S. Nagakura, *In Situ* High Temperature Electron Microscopic Study of the Formation and Growth of Cementite Particles at the Third Stage of Tempering of Martensitic High Carbon Steel, Trans. Jpn. Inst. Met. 26 (1985) 876–885.
[26] P. Matteazzi, F. Miani, G. Le Caër, Kinetics of cementite mechanosynthesis, Hyperfine Interact. 68 (1992) 173–176.
[27] V.A. Barinov, A.V. Protasov, V.T. Surikov, Studying mechanosynthesized Hägg carbide (χ-Fe5C2), Phys. Metals Metallogr. 116 (2015) 791–801.
[28] A. Schneider, G. Inden, Carbon diffusion in cementite (Fe3C) and Hägg carbide (Fe5C2), Calphad 31 (2007) 141–147.
[29] H. Tsybenko, F. Farzam, G. Dehm, S. Brinckmann, Scratch hardness at a small scale: Experimental methods and correlation to nanoindentation hardness, Tribology International 163 (2021) 107168.
[30] S. Brinckmann, G. Dehm, Nanotribology in austenite: Plastic plowing and crack formation, Wear 338-339 (2015) 436–440.
[31] S. Brinckmann, C.A. Fink, G. Dehm, Nanotribology in austenite: Normal force dependence, Wear 338-339 (2015) 430–435.

[32] M.C. Biesinger, B.P. Payne, A.P. Grosvenor, L.W. Lau, A.R. Gerson, R.S. Smart, Resolving surface chemical states in XPS analysis of first row transition metals, oxides and hydroxides: Cr, Mn, Fe, Co and Ni, Applied Surface Science 257 (2011) 2717–2730.

[33] Y. Yang, M.F. Yan, S.D. Zhang, Y.X. Zhang, H.T. Chen, X.A. Wang, One-step plasma-assisted method for functionally graded Fe3O4/DLC coated carburized layer on steel, Diamond and Related Materials 70 (2016) 18–25.

[34] D. Wilson, M.A. Langell, XPS analysis of oleylamine/oleic acid capped Fe3O4 nanoparticles as a function of temperature, Applied Surface Science 303 (2014) 6–13.

[35] P. Ghods, O.B. Isgor, J.R. Brown, F. Bensebaa, D. Kingston, XPS depth profiling study on the passive oxide film of carbon steel in saturated calcium hydroxide solution and the effect of chloride on the film properties, Applied Surface Science 257 (2011) 4669–4677.

[36] B.A. Sosinsky, N. Norem, J. Shelly, Spectroscopic study of a series of iron carbido clusters, Inorg. Chem. 21 (1982) 348–356.

[37] S. Li, H. Yumoto, M. Shimotomai, M. Ishihara, Effects of the power of electron shower and substrate bias on the synthesis of cementite films, Thin Solid Films 345 (1999) 23–28.

[38] C. Yang, H. Zhao, Y. Hou, D. Ma, Fe5C2 nanoparticles: a facile bromide-induced synthesis and as an active phase for Fischer-Tropsch synthesis, Journal of the American Chemical Society 134 (2012) 15814–15821.

[39] C.S. Kuivila, J.B. Butt, P.C. Stair, Characterization of surface species on iron synthesis catalysts by X-ray photoelectron spectroscopy, Applied Surface Science 32 (1988) 99–121.

[40] K. Fan, Z. Jin, J. Guo, Z. Wang, G. Jiang, Investigation on the surface layer formed during electrochemical modification of pure iron, Applied Surface Science 466 (2019) 466–471.

[41] A. Furlan, U. Jansson, J. Lu, L. Hultman, M. Magnuson, Structure and bonding in amorphous iron carbide thin films, Journal of physics. Condensed matter an Institute of Physics journal 27 (2015) 45002.

[42] N. Ochoa, C. Vega, N. Pébère, J. Lacaze, J.L. Brito, CO2 corrosion resistance of carbon steel in relation with microstructure changes, Materials Chemistry and Physics 156 (2015) 198–205.

[43] S. Craig, G.L. Harding, R. Payling, Auger lineshape analysis of carbon bonding in sputtered metal-carbon thin films, Surface Science 124 (1983) 591–601.

[44] A. Schneider, Iron layer formation during cementite decomposition in carburising atmospheres, Corrosion Science 44 (2002) 2353–2365.

[45] B. Lesiak, P. Mrozek, A. Jabloński, A. Jóźwik, Analysis of the Auger KLL spectra of carbon by the pattern recognition method, Surf. Interface Anal. 8 (1986) 121–126.

[46] N.Q. Lam, Physical Sputtering of Metallic Systems by Charged-Particle Impact, Scanning Microscopy (1990).

[47] D. Raabe, P.-P. Choi, Y. Li, A. Kostka, X. Sauvage, F. Lecouturier, K. Hono et al., Metallic composites processed via extreme deformation: Toward the limits of strength in bulk materials, MRS Bull. 35 (2010) 982–991.

[48] S. Andersson, B.G. Hyde, Twinning on the unit cell level as a structure-building operation in the solid state, Journal of Solid State Chemistry 9 (1974) 92–101.

[49] G. Le CaËr, E. Bauer-Grosse, Aperiodic carbides formed by crystallization of amorphous Fe-C alloys, Hyperfine Interact. 47-48 (1989) 55–67.

[50] E. Bauer-Grosse, C. Frantz, G. Le Caer, N. Heiman, Formation of Fe7C3 and Fe5C2 type metastable carbides during the crystallization of an amorphous Fe75C25 alloy, Journal of Non-Crystalline Solids 44 (1981) 277–286.

[51] R. Ghasemi, L. Elmquist, E. Ghassemali, K. Salomonsson, A. Jarfors, Abrasion resistance of lamellar graphite iron: Interaction between microstructure and abrasive particles, Tribology International 120 (2018) 465–475.
[52] M. Mendas, S. Benayoun, Investigating the effects of microstructure on the wear mechanisms in lamellar cast irons via microscratch tests, Tribology International 67 (2013) 124–131.
[53] J.L. do Vale, C.H. Da Silva, G. Pintaude, Tribological performance assessment of lamellar and compacted graphite irons in lubricated ring-on-cylinder test, Wear 426-427 (2019) 471–480.
[54] H.K.D.H. Bhadeshia, Cementite, International Materials Reviews 65 (2020) 1–27.
[55] J. Zhang, A. Schneider, G. Inden, Cementite decomposition and coke gasification in He and H2–He gas mixtures, Corrosion Science 46 (2004) 667–679.
[56] X. Lei, W. Wang, Z. Ye, N. Zhao, H. Yang, High saturation magnetization of Fe 3 C nanoparticles synthesized by a simple route, Dyes and Pigments 139 (2017) 448–452.
[57] K. Kobs, H. Dimigen, C.J.M. Denissen, E. Gerritsen, J. Politiek, L.J. van Ijzendoorn, R. Oechsner et al., Friction reduction and zero wear for 52100 bearing steel by high-dose implantation of carbon, Appl. Phys. Lett. 57 (1990) 1622–1624.
[58] P.J. Wilbur, B.W. Buchholtz, Engineering tribological surfaces by ion implantation, Surface and Coatings Technology 79 (1996) 1–8.